

3 DETECTION OF A $\sim 100,000 M_{\odot}$ BLACK HOLE IN M31'S MOST MASSIVE GLOBULAR CLUSTER: A
4 TIDALLY STRIPPED NUCLEUS

5 RENUKA PECHETTI¹, ANIL SETH², SEBASTIAN KAMANN¹, NELSON CALDWELL³, JAY STRADER⁴, MARK DEN BROK⁵, NORA
6 LUETZGENDORF⁶, NADINE NEUMAYER⁷ & KARINA VOGGEL⁸
7

8 ¹Liverpool John Moores University, UK
9 ²Department of Physics and Astronomy, University of Utah, 115 South 1400 East, Salt Lake City, UT 84112, USA
10 ³Harvard-Smithsonian Center for Astrophysics
11 ⁴Michigan State University, USA
12 ⁵Leibniz-Institut für Astrophysik Potsdam, An der Sternwarte 16, 14482 Potsdam, Germany
13 ⁶European Space Agency, STScI, USA
14 ⁷Max Planck Institut für Astronomie, Heidelberg, Germany
15 ⁸Observatoire astronomique de Strasbourg, USA

16 Draft version October 25, 2021

17 ABSTRACT

18 We investigate the presence of a central black hole (BH) in B023-G078, M31's most massive globular
19 cluster. We present high-resolution, adaptive-optics assisted, integral-field spectroscopic kinematics
20 from Gemini/NIFS that shows a strong rotation (~ 20 km/s) and a velocity dispersion rise towards the
21 center (37 km/s). We combine the kinematic data with a mass model based on a two-component fit to
22 *HST* ACS/HRC data of the cluster to estimate the mass of a putative BH. Our dynamical modeling
23 suggests a $>3\sigma$ detection of a BH component of $9.1_{-2.8}^{+2.6} \times 10^4 M_{\odot}$ (1σ uncertainties). The inferred
24 stellar mass of the cluster is $6.22_{-0.05}^{+0.03} \times 10^6 M_{\odot}$, consistent with previous estimates, thus the BH
25 makes up 1.5% of its mass. We examine whether the observed kinematics are caused by a collection
26 of stellar mass BHs by modeling an extended dark mass as a Plummer profile. The upper limit on
27 the size scale of the extended mass is 0.56 pc (95% confidence), which does not rule out an extended
28 mass. There is compelling evidence that B023-G078 is the tidally stripped nucleus of a galaxy with
29 a stellar mass $>10^9 M_{\odot}$, including its high mass, two-component luminosity profile, color, metallicity
30 gradient, and spread in metallicity. Given the emerging evidence that the central BH occupation
31 fraction of $>10^9 M_{\odot}$ galaxies is high, the most plausible interpretation of the kinematic data is that
32 B023-G078 hosts a central BH. This makes it the strongest BH detection in a lower mass ($<10^7 M_{\odot}$)
33 stripped nucleus, and one of the few dynamically detected intermediate-mass BHs.

34 *Keywords:* galaxies: individual, Andromeda galaxy, galaxies: star clusters, stars: kinematics and
35 dynamics, globular clusters: general, intermediate-mass black holes, galaxies: nuclear star
36 clusters

37 1. INTRODUCTION

38 Intermediate-mass black holes (IMBHs) are hypoth-
39 esized to exist in the mass range between stellar-mass
40 black holes ($\lesssim 100 M_{\odot}$) and super-massive black holes
41 (SMBHs; $\gtrsim 10^5 M_{\odot}$). Some models of SMBH formation
42 rely on stellar or IMBH mass seeds or direct collapse of
43 gas clouds, and thus the detection or lack of IMBHs can
44 help us understand the SMBH formation (e.g. [Greene
45 et al. 2020](#)).

46 Studying IMBHs and the lowest mass SMBHs in galaxy
47 centers can also help in extending and understanding the
48 correlations that exist between galaxies and their black
49 holes (e.g. [Gebhardt et al. 2000](#); [McConnell & Ma 2013](#);
50 [Saglia et al. 2016](#)) to lower masses.

51 Recently, BHs with masses 10^5 - $10^7 M_{\odot}$ have been de-
52 tected in lower-mass galaxies with masses 10^9 - $10^{10} M_{\odot}$
53 using both dynamical measurements ([den Brok et al.
54 2015](#); [Nguyen et al. 2018, 2019](#); [Davis et al. 2020](#)), and
55 measurements of AGN (e.g. [Reines et al. 2013](#); [Chilingarian
56 et al. 2018](#); [Mezcua et al. 2018](#)). SMBHs with
57 masses $>10^6 M_{\odot}$ have also been found at the centers

58 of ultracompact dwarfs (UCDs; e.g. [Seth et al. 2014](#);
59 [Ahn et al. 2017](#)); massive star clusters that appear to
60 be the tidally stripped nuclear star clusters of galax-
61 ies (e.g. [Mieske et al. 2013](#); [Pfeffer & Baumgardt 2013](#);
62 [Neumayer et al. 2020](#)). While so far, these BHs have
63 only been found in the highest mass UCDs ([Voggel et al.
64 2018](#)), there are likely lower mass stripped nuclei and
65 BHs hiding among galaxies' globular cluster (GC) sys-
66 tems ([Voggel et al. 2019](#)). These objects are among the
67 most likely targets for detecting IMBHs.

68 Although GCs are potential reservoirs for IMBHs, de-
69 tecting these IMBHs remains challenging for several rea-
70 sons. First, the gravitational sphere of influence of the
71 IMBHs is small, which limits dynamical IMBH searches
72 (that must resolve this radius) to within the Local Group.
73 Second, dynamical evolution in GCs causes stellar-mass
74 black holes (and more slowly, neutron stars) to mass seg-
75 regate at the center of a cluster. Collections of these
76 stellar remnants can create a rise in the central velocity
77 dispersion mimicking an IMBH (e.g., [Zocchi et al. 2019](#);
78 [Baumgardt et al. 2019](#)). While many stellar-mass BHs
79 will be lost due to interactions or natal kicks, a signifi-

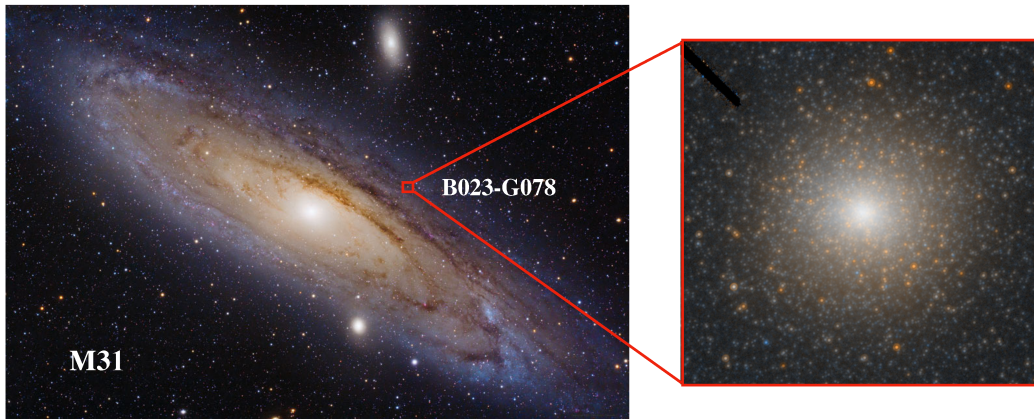


Figure 1. Location and color image of B023-G78. The left panel shows a wide-field image of M31 (Image Credit: Iván Éder, <https://www.astroeder.com/>), with the red box and inset showing the location and HST ACS/HRC image of B023-G78, which is $\sim 10'' \times 10''$.

81 cant fraction of BHs can be retained at the center in some 125
 82 clusters (up to $\sim 2\%$ of the cluster’s mass; Weatherford 126
 83 et al. 2020). Lastly, radial anisotropy can also contribute 127
 84 to creating an observed rise in the central velocity disper- 128
 85 sion without the presence of an IMBH (Zocchi et al. 129
 86 2017). 130

87 There have been claimed dynamical detections of 131
 88 IMBHs in the Milky Way; e.g. in ω Cen (Noyola et al. 132
 89 2010; Baumgardt 2017) ($\sim 4\text{--}5 \times 10^4 M_{\odot}$), M54 (Ibata 133
 90 et al. 2009) ($\sim 10^4 M_{\odot}$), NGC6388 (Lützgendorf et al. 134
 91 2015), but none of these have been proven, and none are 135
 92 supported by evidence for accretion despite very deep 136
 93 radio searches that would be expected to detect even 137
 94 quiescent IMBHs (Tremou et al. 2018). In M31, one of 138
 95 the brightest clusters, G1, has been suggested to contain 139
 96 an IMBH of $\sim 2 \times 10^4 M_{\odot}$ (Gebhardt et al. 2002, 2005); 140
 97 however this detection is also controversial (Baumgardt 141
 98 et al. 2003), and a lack of accretion evidence was shown 142
 99 in Miller-Jones et al. (2012). 143

100 Yet, despite the challenges of IMBH detection in GCs, 144
 101 it appears that at least some IMBHs do exist (see re- 145
 102 cent review by Greene et al. 2020). The most convincing 146
 103 detection of an IMBH is the bright, off-nuclear X-ray 147
 104 source HLX-1. This object, found ~ 3 kpc from the cen- 148
 105 ter of a massive galaxy has an estimated BH mass of 149
 106 a few $\times 10^4 M_{\odot}$ (Davis et al. 2011; Webb et al. 2012; 150
 107 Godet et al. 2012; Straub et al. 2014). This source ap- 151
 108 pears to be surrounded by a star cluster as well (Farrell 152
 109 et al. 2014). 153

110 In this paper, we use high-resolution mass models and 154
 111 kinematics to present the detection of a $\sim 10^5 M_{\odot}$ IMBH 155
 112 with $> 3\sigma$ significance in B023-G78. This cluster is 156
 113 the most massive GC in M31, with a dynamical mass 157
 114 of $6.8_{-0.6}^{+0.7} \times 10^6 M_{\odot}$ and a central dispersion of 33.0 ± 1.8 158
 115 km/s (Strader et al. 2011), and is located along the mi- 159
 116 nor axis of M31 at a projected distance of 4.4 kpc to- 160
 117 wards its center (Figure 2). Line index measurements 161
 118 by Caldwell et al. (2011) suggest a metallicity $[\text{Fe}/\text{H}] =$ 162
 119 -0.7 , while analysis of the width of the RGB suggests 163
 120 a significant metallicity spread (Fuentes-Carrera et al. 164
 121 2008). The reddening is uncertain due to a dust lane 165
 122 passing in front of this GC with values ranging from 166
 123 $0.23 - 0.43$, we use the $E(B-V)$ value of 0.23 (Jablonka 167
 124 et al. 1992) as our default value. We also assume the

values $A_{F814W}/A_V = 0.59$ and $A_{F606}/A_V = 0.91$. Sur-
 face brightness profile fits performed by Barmby et al.
 (2007) using a single King profile suggests a core and
 tidal radius of 1.35 pc and 37.15 pc, respectively (and
 thus an effective radius of $3.7 \text{ pc}/1.0''$). We assume the
 distance of M31 (and also to B023-G78) to be 0.77 Mpc
 (Karachentsev et al. 2004). All the magnitudes in this
 paper are expressed in Vega magnitudes.

In § 2 we present the imaging and spectroscopic data.
 § 3 and § 4 describe the surface photometry and the dy-
 namical modeling performed on the cluster. § 5 presents
 our discussion and conclusions.

2. DATA

2.1. HST Data

We used archival *HST* data for this cluster from
 the proposal ID:9719 (PI: T. Bridges)¹. The observa-
 tions were performed with the Advanced Camera for
 Surveys/High-Resolution Camera (ACS/HRC) in the fil-
 ters F814W and F606W. The exposure times were 2860 s
 and 2020 s respectively.

The ACS/HRC has a pixel scale of $0.025''/\text{pixel}$ and
 a field of view of $29'' \times 26''$. We downloaded the individ-
 ual .flt files from Mikulski archive for space telescopes
 (MAST) and drizzled them using Astrodrizzle (Gon-
 zaga et al. 2012) to create the final image. The MDRIZSKY
 keyword was set to zero to avoid over-subtraction of the
 sky in the final drizzled image. The final color image
 (F606W - F814W) is shown in the right panel of Fig-
 ure 1.

The drizzled PSF in each band was obtained by insert-
 ing Tiny Tim PSFs into mock .flt images and drizzling
 them the same way as the science image. This procedure
 is similar to the one described in Pechetti et al. (2020).
 We note that the F814W PSF has a significant amount
 of light in a large halo; a PSF of radius $5''$ was used to
 account for this.

2.2. Gemini/NIFS Data and Kinematics

We obtained Gemini/NIFS laser guide star adap-
 tive optics observations of B023-G78 on Oct. 7 and

¹ The specific observations can be accessed via [doi:10.17909/t9-pm76-g165](https://doi.org/10.17909/t9-pm76-g165)

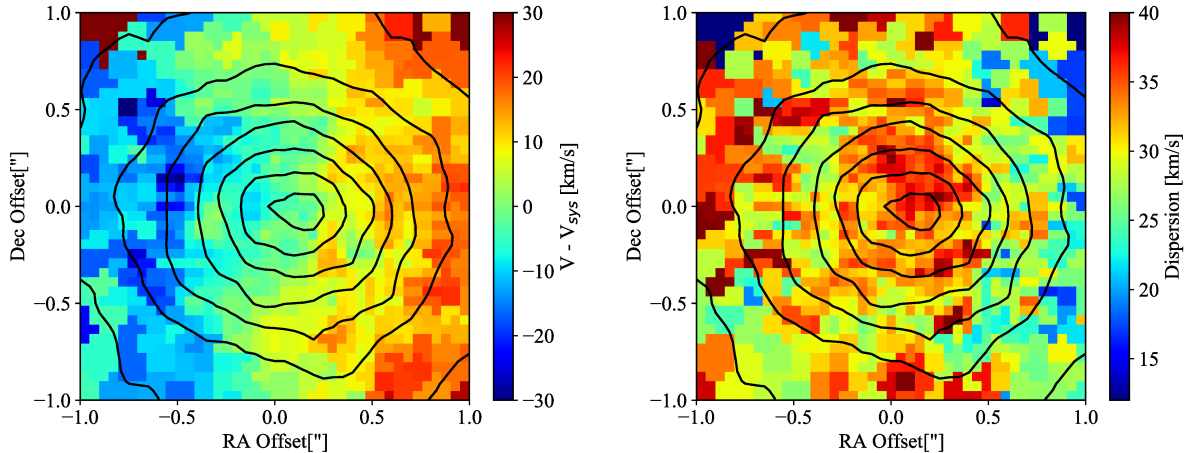


Figure 2. Kinematics of B023-G78. The above two panels are the stellar kinematic maps (velocity and velocity dispersion respectively) of the cluster derived from adaptive optics assisted Gemini/NIFS data. The systemic velocity (V_{sys}) was estimated to be -435 km/s.

164 Nov. 9 2014 as part of program GN-2014B-DD-2 204
 165 (PI: A.C. Seth). The data provides integral field spec- 205
 166 troscopy in the H band ($1.48\text{--}1.79\mu\text{m}$) over a field of view 206
 167 of $3''$ (11 pc at 0.77 Mpc). For our final data cube with a 207
 168 spaxel size of $0.05''$, we combined the 6/8 900s dithered 208
 169 exposures using the Gemini IRAF packages, with modifi- 209
 170 cations as described in Seth et al. (2010); Ahn et al. 210
 171 (2018). Despite the use of offset sky exposures, addi- 211
 172 tional on-chip sky subtraction was required before combi- 212
 173 nation, using the corners of the chip; this makes our use- 213
 174 ful field of view $\sim 2''$. The line spread function was mea- 214
 175 sured from sky lines in each pixel with a median FWHM 215
 176 of 3.27\AA . The kinematic maps are shown in Figure 2. 216

177 Due to the data's high-spatial-resolution, we were able 217
 178 to resolve individual stars in the GC. To mitigate shot- 218
 179 noise effects due to the brightest cluster stars, we used 219
 180 the PampelMuse software (Kamann et al. 2013) to gener- 220
 181 ate a star subtracted cube of the GC. To describe 221
 182 the method in short, we fitted a single Sérsic image to 222
 183 the continuum image of the cluster and inspected the 223
 184 fit residuals. We then manually identified the locations 224
 185 where the residuals suggested the presence of resolved 225
 186 stars and the resulting list was used to recover their PSFs 226
 187 as a function of wavelength using PampelMuse (Kamann 227
 188 et al. 2013). These PSF and the positions were used to 228
 189 extract the spectra of the input stellar sources. Finally, 229
 190 we combined the wavelength-dependent PSF model with 230
 191 the positions and the extracted spectra of the resolved 231
 192 stars to subtract their contributions from the NIFS data. 232

193 In deriving the stellar kinematic maps, we first per- 233
 194 formed Voronoi binning using the code from Cappellari 234
 195 & Copin (2003). After resampling the integral field spec- 235
 196 troscopic data into bins of $S/N = 50$, we estimate the 236
 197 kinematics in each bin using the penalized pixel fitting 237
 198 (pPXF) algorithm and code as described in Cappellari 238
 199 (2017). This code uses the full spectrum ($1.5\mu - 1.8\mu$) 239
 200 to fit the radial velocity (V), and velocity dispersion 240
 201 (σ_e). We used 65 Phoenix stellar templates from Husser 241
 202 et al. (2013)² with metallicities ranging from -1 to 0 , $\log(g)$ 242
 203 from $1 - 5.5$, temperatures from $3600 - 5500$ K, and 243

204 $[\alpha/\text{Fe}]$ from $0 - 0.4$, covering the range of parameters 205
 206 expected to dominate the light in B023-G78. To esti- 207
 208 mate the kinematic errors, we performed Monte Carlo 209
 210 simulations by adding a random Gaussian error to the 211
 212 spectrum in each bin and re-fitting the kinematics. The 213
 214 standard deviation of those fits was taken as 1σ un- 215
 216 certainties. The final derived kinematics are shown in 216
 217 Figure 2. The central velocity dispersion is ~ 37 km/s, 218
 219 while clear rotation is seen around the minor axis with 220
 221 an amplitude of ~ 20 km/s and a systemic velocity of 222
 223 ~ -435 km/s. The integrated dispersion out to $1''$ is 224
 225 34.2 km/s; this is in reasonable agreement with the ob- 226
 227 served value of 31.7 ± 1.7 km/s by Strader et al. (2011) 228
 229 using higher spectral resolution optical spectroscopy at 229
 230 seeing limited spatial resolution. 230

2.3. Deriving the kinematic PSF

231 To perform dynamical modeling with precision, under- 232
 233 standing the PSF of the Gemini/NIFS kinematic data is 233
 234 critical. To determine the PSF, first, we astrometrically 234
 235 aligned a continuum image created from the NIFS data 235
 236 cube (created without the additional on-chip sky sub- 236
 237 traction) to the HST F814W image. Then, we used the 237
 238 HST F814W image within a $1''$ radius and convolved it 238
 239 with a double Gaussian model of the PSF, varying the 239
 240 parameters of the Gaussians until the convolved HST 240
 241 image best matched the continuum image created from the 241
 242 data cube. We then convolved the resulting PSF model 242
 243 with the HST PSF to obtain the widths and relative 243
 244 strengths of the two Gaussian components. The best-fit 244
 245 FWHM of the inner and outer Gaussian component was 245
 found to be $0.127''$ containing 31.4% of the total light, 246
 and $0.58''$ containing 68.6% of the light, respectively. 246

247 To account for systematic errors arising from the PSF 247
 248 model (described in § 4.3), we also created PSFs with 248
 249 different sets of inputs. We estimated a PSF as described 249
 250 above, but fitted the F814W image out to a larger radius 250
 251 ($1.35''$). Another PSF was generated as above but using 251
 252 the F606W HST image. The parameters of the PSFs in 252
 253 both the cases agreed within $\sim 10\%$ in the FWHMs and 253
 254 ratios of the components. This consistency is likely due 254
 255 to the lack of a strong color gradient seen in this cluster 255

² <http://phoenix.astro.physik.uni-goettingen.de/>

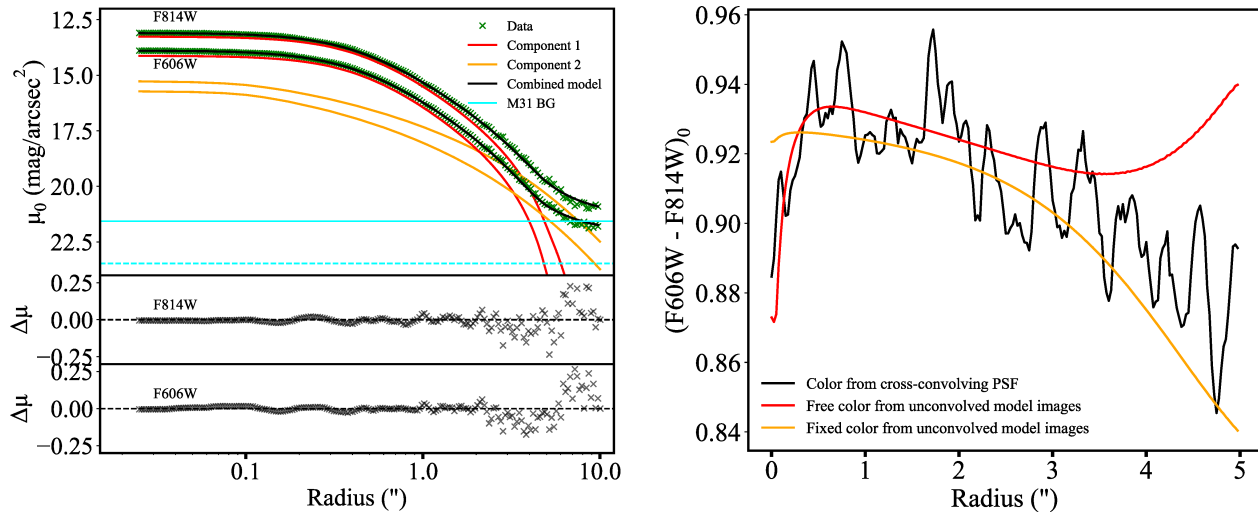


Figure 3. Surface brightness profile and color of B023-G78. **Left:** Best-fit model (King + Sérsic) decomposition of the surface brightness of B023-G78 in F814W and F606W from the ACS/HRC data; note that surface brightnesses are in Vega magnitudes. The blue (solid and dashed) is the M31 background estimated using SDSS images (in F814W and F606W respectively; § 3). The residuals (Data - Model) are shown in the bottom panels. **Right:** Color map derived by convolving the PSF of F814W to the F606W image and vice-versa (in black). The orange line is the color from the unconvolved model images, where the parameters of F814W were fixed to the best-fit model parameters of F606W, therefore requiring that the two components each have a unique color. The red line is the color when the fit parameters in both the F814W and F606W were allowed to be free. **The magnitudes in the right panel are extinction corrected with an $E(B-V)$ of 0.23.**

246 (see next section).

247 3. CREATING LUMINOSITY MODELS

248 We fit the HST based surface brightness (SB) profiles
 249 of the cluster using the IMFIT code (Erwin 2015).
 250 The code builds a 2-D model image using the input param-
 251 eters and then convolves it with the given PSF. The best-
 252 fit χ^2 is then estimated to find the closest model of the
 253 galaxy. Our best-fit model has two components, an in-
 254 ner King profile, and an outer Sérsic profile. The King
 255 profile (King 1962) is described by the central intensity
 256 (I_0), tidal radius (r_t), and core radius (r_c); although the
 257 IMFIT code uses a generalized King profile (Peng et al.
 258 2010), we fix the power-law index α set to 2 to obtain
 259 the standard empirical King profile. The Sérsic profile
 260 (Sersic 1968; Graham & Driver 2005) is described by the
 261 Sérsic index (n), effective radius (r_e), and the intensity
 262 at the effective radius (I_e). Apart from these input pa-
 263 rameters to the models, we also provide position angle
 264 (PA), which is defined as the angle of the semi-major
 265 axis measured north through east counter-clockwise and
 266 ellipticity (ϵ) as free parameters for each component to
 267 fit the 2-D image of the cluster.

268 The image also includes background light from M31,
 269 which we assume is locally flat. We estimated the back-
 270 ground from M31 and the sky levels of the HST images
 271 (which are not sky subtracted) by matching the SBs of
 272 the large-scale SDSS images in r and i bands transformed
 273 to HST F606W and F814W Vega magnitudes. After fit-
 274 ting for the HST image background levels, the trans-
 275 formed SDSS and HST SB profiles matched well beyond
 276 a radius of $5''$. To obtain the M31 background we used
 277 the mean surface brightness value in the region of 12–
 278 $18''$ from the SDSS image and incorporated this as a flat
 279 background component in our models. We estimated this
 280 background level to be at 21.57 and 22.59 mag/arcsec²

281 in F606W and F814W respectively. The standard devi-
 282 ation in the SDSS surface brightness at large radii was
 283 taken as the 1σ error on this estimate; ~ 0.05 mags in
 284 both bands.

285 The SB profile fits were performed separately in both
 286 the F814W and F606W filters. Here, the fitting param-
 287 eters were allowed to vary. To estimate the change in
 288 the color of the cluster in the model images, we fixed the
 289 best-fit model parameters of the F814W image to that
 290 of the F606W image; we found an $(F606W-F814W)_0$ of
 291 0.94 mags for the inner component and 0.89 mags for the
 292 outer component. A 1-D radial profile of the cluster's
 293 surface brightness and the model fit is shown in the left
 294 panel of Figure 3, which was derived from summing up
 295 the 2-D image in annuli of increasing radii. The best-fit
 296 parameters are given in Table 1. We note that Barmby
 297 et al. (2007) show that a single Wilson profile provides
 298 a good fit to the 1-D profile of B023-G78. However, the
 299 combination of the outer component's bluer color and
 300 its significantly higher ellipticity indicates a real physical
 301 difference in the two components.

302 As noted earlier, the F814W PSF has a red halo, and
 303 thus to examine the color profile in more detail, we cre-
 304 ated a cross-convolved color map, i.e. we convolved the
 305 F814W image with the PSF of F606W and vice versa.
 306 The resulting color profile is shown in the right panel of
 307 Figure 3. We show the central $5''$, out to the radius of
 308 our PSF. The observed color gradient roughly matches the
 309 expectations from our fixed parameter fits, with a
 310 ~ 0.05 mag decline between the central arcsecond and $5''$.
 311 Because this color gradient is so small, especially over the
 312 area we are fitting, we assume a constant M/L in our dy-
 313 namical models, but we also explore mass models with a
 314 varying M/L in § 4.3. The theoretical color for a popula-
 315 tion of 10 Gyr and $[Fe/H]$ of -0.7 is ~ 0.82 mags using the
 316 PARSEC models (Bressan et al. 2012). This is consider-

Table 1
Best-fit parameters in F814W and F606W for B023-G78

| Function | Parameter | Best-Fit values | |
|-------------------|---------------------|---------------------------------------|---------------------------------------|
| | | F814W | F606W |
| King | $\log I_0$ | 4.91 L_\odot/pc^2 | 4.65 L_\odot/pc^2 |
| | r_c | 2.69 pc | 2.68 pc |
| | $c = \log(r_t/r_c)$ | 1.11 | 1.12 |
| | ϵ | 0.10 | 0.11 |
| | PA | 80.0 | 76.4 |
| | mag_{tot} | 13.02 | 14.22 |
| Sérsic | $\log I_e$ | 1.79 L_\odot/pc^2 | 1.24 L_\odot/pc^2 |
| | r_e | 18.74 pc | 15.06 pc |
| | n | 2.56 | 2.52 |
| | ϵ | 0.24 | 0.26 |
| | PA | 77.0 | 85.6 |
| | mag_{tot} | 14.08 | 15.24 |
| M31 background | | 21.57 $\text{mag}/\text{arcsec}^2$ | 22.59 $\text{mag}/\text{arcsec}^2$ |
| Half-light radius | r_{hl} | 4.23 pc | |

Note: The cluster is fitted by a King + Sérsic model. The parameters and their corresponding best-fit values are shown here. These parameters are from the free models. The magnitudes and luminosities are not extinction corrected.

Table 2
Best-fit MGE parameters of F814W fits for B023-G78

| Intensity (L_\odot/pc^2) | Gaussian width (arcsec) | Axial ratio |
|--|----------------------------|-------------|
| 24526 | 0.19 | 0.90 |
| 2307 | 0.24 | 0.90 |
| 43610 | 0.40 | 0.90 |
| 11092 | 1.06 | 0.90 |
| 4396 | 0.07 | 0.76 |
| 3435 | 0.13 | 0.76 |
| 2278 | 0.23 | 0.76 |
| 694 | 0.29 | 0.76 |
| 1478 | 0.39 | 0.76 |
| 392 | 0.46 | 0.76 |
| 1169 | 0.62 | 0.76 |
| 805 | 0.90 | 0.76 |
| 252 | 1.14 | 0.76 |
| 190 | 1.34 | 0.76 |
| 454 | 1.67 | 0.76 |
| 288 | 2.80 | 0.76 |
| 1.40 | 3.13 | 0.76 |
| 84.4 | 5.77 | 0.76 |

Note: The MGE parameters for the fits to the F814W data in Table 1.

sian components as described in Table 2. The ellipticities from the IMFIT models were converted to axial ratios to deproject these MGEs.

4. DYNAMICAL MODELING AND BH MASS ESTIMATES

In this section, we present dynamical models of B023-G078 that focus on constraining the mass of a possible central BH mass using Jeans' anisotropic modeling (JAM; Cappellari 2008). We first present results for our default model, then explore the impacts of the uncertain extinction correction and possible systematic errors on our best-fit models. We present additional dynamical models exploring the possibility of a cluster of stellar mass black holes in § 5.2.

4.1. Results from Jeans Anisotropic modeling

For estimating the BH mass, we used the JAM method for our dynamical models. These models use the 3-D deprojected MGE densities that were derived from the HST data in the previous section to create a gravitational potential. To this potential, a BH assuming a Gaussian potential with a very small scale ($\sim 0.01''$) is added. Using the potential and MGEs, the Jeans' equations are solved to estimate an intrinsic value of the root mean square (RMS) velocity ($V_{RMS} = \sqrt{(V - V_{sys})^2 + \sigma_0^2}$), where V is the rotation velocity, V_{sys} is the systemic velocity, and σ_0 is the velocity dispersion. The estimated V_{RMS} is then integrated along the line of sight to compare with the observed RMS velocities derived from the Gemini/NIFS data out to a radius of $1''$. Our default model uses the kinematic PSF derived from fitting the Gemini/NIFS data to the F814W image, the best-fit two-component King+Sérsic model derived from the F814W image (Table 1), and the kinematics data cube after star subtraction. We discuss additional models used to assess our systematic errors in § 4.3.

We explore our JAM model fits by varying the following 4 free parameters: mass-to-light ratio (M/L), inclination angle (i), anisotropy parameter β , and BH mass M_{BH} , since they are degenerate. We estimate the best-fit values by sampling the parameter space using Markov Chain Monte Carlo (MCMC) simulations with the `emcee` package (Foreman-Mackey et al. 2013). We ran our models for 10000 iterations. The resulting posterior probability distribution functions of our model parameters are shown in Figure 4.

We obtain a best-fit BH mass of $9.1_{-2.8}^{+2.6} \times 10^4 M_\odot$. The χ^2 of the best-fit model is 404. The best-fit no-BH model has a $\Delta\chi^2$ of 30, excluding this model at $> 3\sigma$ significance relative to the model with a BH. We estimated the Bayesian information criterion (BIC) for the best-fit IMBH model and the no-BH model. The ΔBIC was 24, which provides strong evidence against the no-BH model. **A $\Delta\text{BIC} > 10$ supports strong evidence for one model over another (Kass & Raftery 1995).** For the best-fit BH mass and σ_e as the integrated velocity dispersion at $\sim 0''.5$, the sphere of influence radius ($\text{SOI} = GM_{BH}/\sigma_e^2$) is ~ 0.33 pc or $\sim 0''.09$; for comparison, the PSF core sigma (FWHM/2.35) is $0''.055$, thus the SOI is resolved by our kinematic data as expected given the $> 3\sigma$ significance of the BH mass detection. The best-fit M/L_{F814W} is $1.87_{-0.04}^{+0.04}$, giving a total dynamical mass

ably bluer than the observed and model colors, suggesting that our assumed reddening, $E(B-V)=0.23$ (Jablonska et al. 1992), may be underestimated. We discuss this further in § 4.2.

We use multi-Gaussian expansion (MGE) models to deproject the SB profiles for use in dynamical models. This method is described in detail in Pechetti et al. (2020). In short, we used the best-fit parameters from Table 2 and converted them to MGE models using the `mge_fit_1d` code (Cappellari 2002), sampling the SB profile logarithmically. The final model contains 18 Gaus-

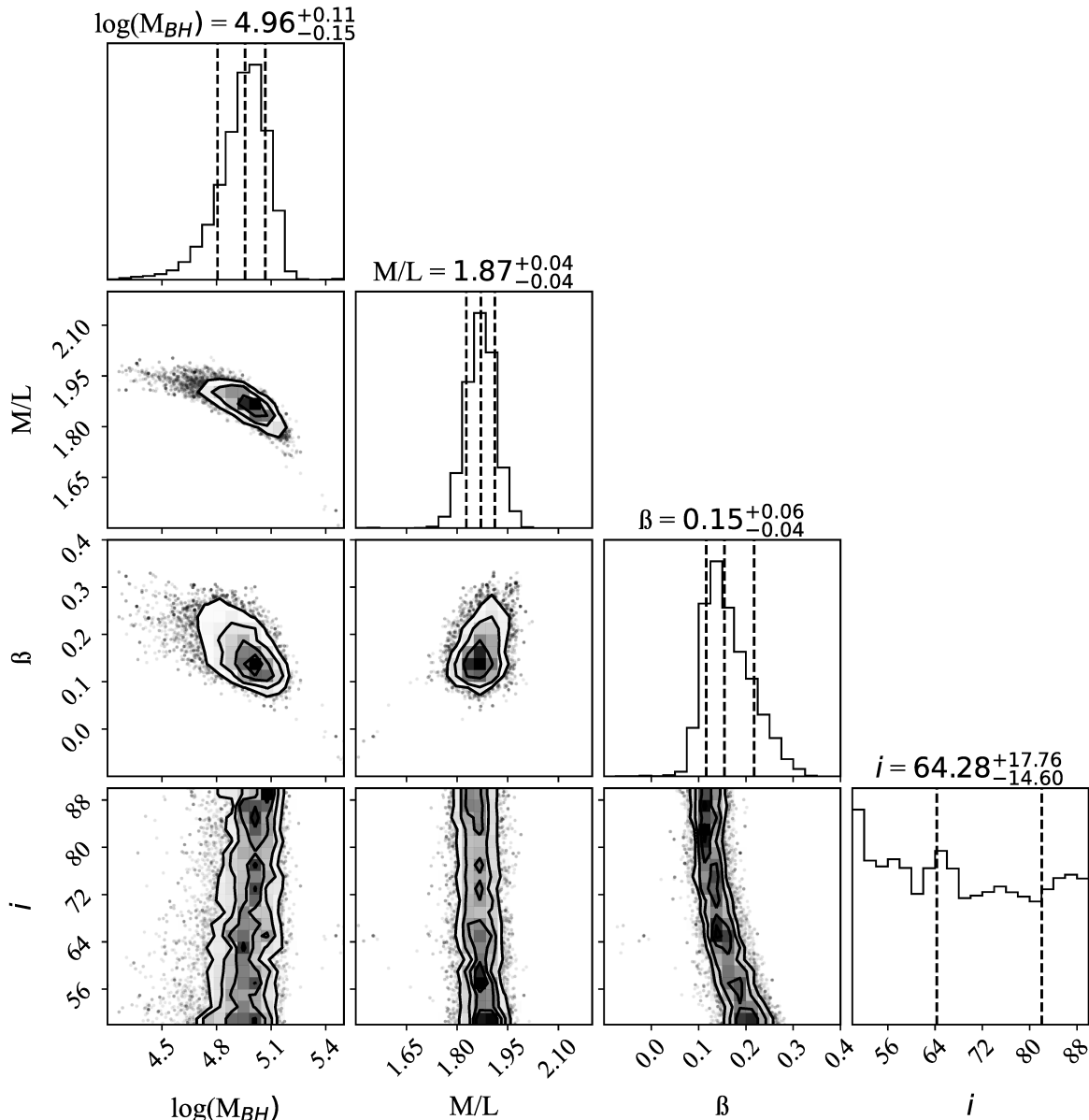


Figure 4. The output of JAM models from MCMC simulations showing the best-fit BH mass. M_{BH} gives the black hole mass, M/L indicates the mass-to-light ratio in the F814W band, β shows the anisotropy, and i gives the inclination. The top panel shows the probability distribution function of the black hole mass marginalized over all other parameters.

390 of $6.22 \times 10^6 M_{\odot}$ for this cluster. This total dynamical
 391 mass is similar to that found in [Strader et al. \(2011\)](#)
 392 ($6.8^{+0.7}_{-0.6} \times 10^6 M_{\odot}$). We discuss the uncertainties in the
 393 M/L due to extinction in the next subsection but note
 394 that the dynamical mass is robust to changes in extinc-
 395 tion. The models also suggest moderate radial anisotropy
 396 with a best-fit β of $0.15^{+0.05}_{-0.03}$. The inclination is not well
 397 constrained, but does not affect the estimates of other
 398 parameters. To visualize the models and data better,
 399 Figure 5 shows a 1-D radial profile of the measured annu-
 400 lar V_{RMS} and the V_{RMS} model prediction, as well as
 401 showing the best-fit model without a BH. The model 1-D
 402 profiles are estimated by creating radial bins from the
 403 2-D model and taking the median for each bin along the
 404 major axis of the cluster. Every iteration of the MCMC
 405 simulation within 1σ is also plotted, which is the shaded

408 region.

4.2. Effects Of Extinction

409 As noted in the introduction, the dust lane passing in
 410 front of this cluster makes the extinction of this cluster
 411 poorly known. This uncertainty translates directly
 412 into an uncertainty in the M/L of the cluster, however,
 413 the BH mass and total dynamical mass of the cluster
 414 are not sensitive to changes in the extinction because
 415 these are constrained by the combination of the kine-
 416 matics and the shape of the mass model. To check for
 417 any extinction variations within the cluster, we averaged
 418 the color of the cluster azimuthally, but there were min-
 419 imal variations ($<1\%$). This suggests that the extinc-
 420 tion is nearly constant in the region we are modeling.
 421 Our default reddening of $E(B-V)=0.23$ (corresponding

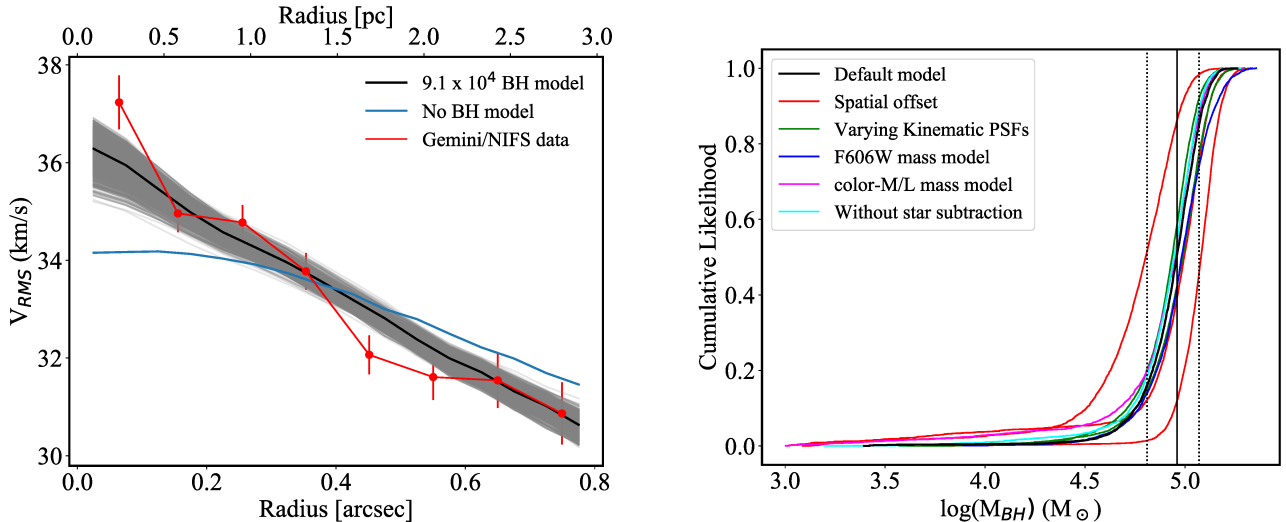


Figure 5. Left: A 1-D profile of the observed kinematics compared to model fits. Red points show annular V_{RMS} values from Gemini/NIFS. The black line shows the best-fit BH mass model with gray lines showing other models from the MCMC model fits. The blue line is the best-fit no-BH model derived from fitting only 3 parameters (M/L , i and β). Right: Cumulative likelihood of the BH mass estimate. The default model is the black solid line. The dashed lines are the 1σ uncertainty levels. We also show other models to highlight the level of systematic error in our default model. This includes mass model variations (i.e. using the F606W image fits and varying the M/L based on the color of the components), spatial offsets of one NIFS pixel, fits to kinematics derived from data cubes without star subtraction, and fits where we vary the kinematic PSF. All but the spatial offsets result in changes at the $<1\sigma$ level of the black hole mass, while the spatial offsets (which are significantly larger than our uncertainties in the center) are consistent within 2σ with the black hole mass in the default model.

to $A_{F814W} = 0.427$) from Jablonka et al. (1992) provides an M/L of ~ 1.9 ; the range of I band mass-to-light ratios observed in other M31 clusters is $\sim 1-2$ for high mass clusters with similar metallicity (calculated from Peacock et al. 2010; Strader et al. 2011), thus our derived value is reasonable, although a bit on the higher side. Using a higher reddening value in our dynamical modeling, like the $E(B-V) = 0.43$ from Caldwell et al. (2011) gives an $M/L_{F814W} = 1.35$, also still within the range of observed M/L s. We also analyzed the resolved photometry in our HST data. Comparison of this data to Parsec isochrones (Bressan et al. 2012) suggests the CMD position of the RGB and red clump stars are consistent with $E(B-V) = 0.23$, and rule out significantly higher reddenings. We therefore use the Jablonka et al. (1992) value as our default value. We note that our choice of reddening/extinction does not impact the dynamical estimates of the best-fit BH mass or the total stellar mass of the cluster.

4.3. Sources of Systematic Error

Several systematic errors can affect our dynamical models. We discuss each of these and summarize their effect on our estimated BH mass in the right panel of Figure 5. The default model as mentioned in the previous section is depicted in the black line.

One source of uncertainty in dynamically modeling GCs is defining the center (e.g. Noyola et al. 2010; Anderson & van der Marel 2010). When determining the surface photometry, IMFIT fits the center along with the cluster surface brightness. The formal error on the center was 0.156 mas, which underestimates the true uncertainty. We also estimated the center by running the ELLIPSE task using IRAF. We did not fix the center and estimated the center using ellipses with semi-major axes

of $0.2''-3''$. We then determined the standard deviation of the measurements, which was ~ 12.5 mas. Given that this is $\sim 1/4$ th the size of the kinematic pixels, this uncertainty has minimal impact on our dynamical models. Despite the small apparent uncertainty in our center, we tested the impact on the BH mass by shifting the central position of the cluster by $0.05''$ (1 NIFS pixel), in the x and y direction. The resulting variations in the cumulative distribution function of the inferred BH mass, shown as the red lines in Figure 5, were fairly large but still within the 2σ uncertainty of our default model (black line). Note that to get the center of kinematics to match that of the HST data, during our PSF analysis, we obtain the best-fit astrometry matching our NIFS data to the HST images.

Another major source of potential systematic error is the kinematic PSF that we derive using a double Gaussian profile. As described in § 2.3, we estimated the PSFs using different fitting radii on the F814W image, and using the F606W image. The impact of the PSF on our results is shown with green lines in Figure 5.

The luminosity/mass models we use also have two types of uncertainties: (1) uncertainties in the parameterization of the SB profiles, and (2) the possibility that the M/L varies with radius, invalidating the mass-traces-light assumption in our first model. This could be due to varying stellar populations in the cluster (which we explore here) or due to mass segregation (discussed in the next subsection). To explore the size of uncertainties in (1) we use the best-fit F606W King+Sérsic model; this is shown as blue line in Figure 5, which again did not create much variation in the BH mass. To explore (2), we performed tests by varying the M/L in our mass model instead of assuming a constant M/L . We assigned a M/L for the King and the Sérsic components based on their integrated colors using the theoretical color- M/L relations

from Roediger & Courteau (2015). These were then used as an input in our JAM models, and a single mass-scaling factor was used in place of the M/L (as in Nguyen et al. 2018, 2019). This did not create much variation in the BH mass (shown as the pink line in Figure 5).

Finally, we used the original kinematics data cube rather than the one after star subtraction to estimate the BH mass but there was not much variation observed (shown as a cyan line in Figure 5). Overall, these tests suggest that the dynamical signature of the IMBH in B023-G78 is robust.

Based on all the systematic errors that we explore, we find that none of them substantially change the estimated BH mass.

5. DISCUSSION

We first discuss the evidence that B023-G078 is a stripped nucleus, and the interpretation of our BH results in that context. We then consider a collection of stellar-mass BHs as an alternative to the IMBH interpretation, and finish by examining B023-G078 in a broader context.

5.1. Additional Evidence that B023-G78 is a Stripped Nucleus

The presence of an IMBH might be expected in B023-G78 if it is a stripped nuclear star cluster (NSC) of a once more massive galaxy (e.g. Pfeffer & Baumgardt 2013). B023-G78 is the most massive cluster in M31 and an outlier in the M31 globular cluster luminosity function (Barmby et al. 2001; Strader et al. 2011). **In the Milky Way, there is strong evidence that some of the most massive clusters are stripped NSCs. ω Cen consists of complex stellar populations that cover a broad metallicity distribution. In addition, it has recently been suggested as the former core of Sequoia or Gaia-Enceladus galaxy (e.g. Majewski et al. 2012; Myeong et al. 2019; Simpson et al. 2020; Pfeffer et al. 2021). The NSC of the tidally disrupting Sagittarius dwarf galaxy, M54, provides evidence that this stripping process is ongoing. It also shows complicated star formation history and a spread in metallicity and ages of the stars (e.g. Sarajedini & Layden 1995; Siegel et al. 2007; Alfaro-Cuello et al. 2019; Pfeffer et al. 2021). All of the globular cluster formation mechanisms are unable to explain these observations (e.g. Bastian & Lardo 2018).** Assuming B023-G078 is a stripped NSC, we estimate a galaxy progenitor stellar mass of $5.3 \times 10^9 M_{\odot}$ using the galaxy-NSC mass relation from Neumayer et al. (2020); this relation has significant scatter, but most known NSCs of B023's mass are hosted in galaxies above $10^9 M_{\odot}$. In this range of galaxy stellar masses the black hole occupation fraction is high (Nguyen et al. 2019; Greene et al. 2020).

The metallicity (e.g. Janz et al. 2016) and metallicity spread (e.g. Pfeffer et al. 2021) of a globular cluster can provide additional evidence for a stripped NSC. The metallicity of B023-G078 has been estimated to be roughly -0.7 from several studies of both spectra and CMDs (Fuentes-Carrera et al. 2008; Perina et al. 2009; Caldwell et al. 2011). The observed metallicity for B023-G078 is within the observed range of NSC metallicities in its inferred host galaxy mass range (Neumayer

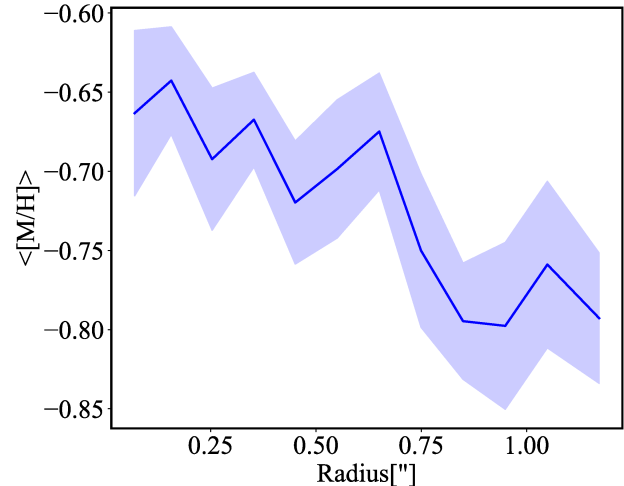


Figure 6. A clear metallicity gradient is seen in our Gemini/NIFS data. We fit annular spectra using A-LIST models (Ashok et al. 2021) to determine the light-weighted mean metallicity as a function of radius. Error bars are based on Monte Carlo simulations.

et al. 2020). Furthermore, the large spread in metallicities inferred from color-magnitude diagram modeling by Fuentes-Carrera et al. (2008) provides strong evidence for B023-G078 being a stripped nucleus with a range of metallicities similar to M54 (Alfaro-Cuello et al. 2019) or ω Cen (Johnson & Pilachowski 2010). The fits to APOGEE near-infrared spectra presented in Ashok et al. (2021) find a best-fit metallicity of $-0.5^{+0.3}_{-0.1}$, a best-fit $[\alpha/M]$ of +0.1, and a considerably younger age (~ 6 Gyr) than any of the other 32 M31 GCs analyzed; this younger population also is suggestive of a stripped NSC where young populations are expected to form until the epoch of stripping (Neumayer et al. 2020).

Given our observed color gradient and the previously observed metallicity spread, we analyzed our NIFS spectra in radial annuli to detect any significant age or metallicity gradient in B023-G078. The spectra were binned into 12 annuli with a maximum radius of $1''.25$ with S/N ranging from >200 near the center to ~ 80 at the largest radii. We then fit the spectra using pPXF with the A-LIST spectral models, a set of simple stellar population templates created using APOGEE spectra (Ashok et al. 2021). We selected Padova-based templates with $[\alpha/M]=0.1$, ages ranging from 2 to 12 Gyr, and $[M/H]$ from -2 to +0.4. The fits were very good, although due to the high S/N , the reduced χ^2 was as high as 2.5 in the inner part of the cluster. A light-weighted mean metallicity and age were calculated at each radius, and then a Monte Carlo analysis was run to determine the errors on these quantities (note that the error spectra were scaled by $\sqrt{\chi^2}$ of the best-fit at each radius during this analysis). The light-weighted metallicity is consistent with previous metallicity determination and shows a clear negative gradient of ~ 0.15 dex between the center and $1''$ as shown in Figure 6. The light-weighted age is found to be 10.5 ± 0.5 Gyr with no significant gradient.³ The lower metallicities at larger radii are also consistent with the

³ This age is significantly older than the value measured by Ashok et al. (2021) using the same models but independent data. We note that if we force a younger age on our fits, we get slightly worse fits, and higher metallicities consistent with the -0.5 found

bluer colors of our outer component inferred in our model fits to the B023-G078. The observed metallicity gradient is similar to those seen in ω Cen and M54 (e.g. Suntzeff & Kraft 1996; Monaco et al. 2005) with the metal-rich populations being more concentrated than the metal-poor populations. Overall, we interpret the metallicity spread and gradient as evidence of the multiple generations of stars we expect to see in NSCs.

We note two additional pieces of evidence that favor B023-G078 being a stripped NSC. First, the strong rotation ($V/\sigma \approx 0.8$) seen is typical of NSCs (Neumayer et al. 2020), but is higher than those seen in Milky Way GCs (Kamann 2018); note that this value is a lower limit due to the unknown inclination of the system. Second, the two-component structure of the cluster is as expected from a stripped NSC (Pfeffer & Baumgardt 2013), and is similar to the more massive UCDS with known BHs (Seth et al. 2014; Ahn et al. 2017, 2018). The apparent (weak) color variation between the two components is also consistent with NSCs, where stellar population variations and gradients are expected (Neumayer et al. 2020). Overall, there is strong evidence that B023-G078 is in fact a stripped nucleus from a galaxy in a mass range where central BHs are commonly found.

5.2. Possible alternatives to a central IMBH

Dynamical evolution is expected to increase the M/L of clusters both at the center, due to the mass segregation of BHs and neutron stars, and in the outer parts, due to kicks received by low-mass dwarf stars (e.g. den Brok et al. 2014; Baumgardt 2017). The mass segregation of the remnants happens on a timescale less than the half-mass relaxation time, which in B023-G78 is ~ 14 Gyr, and thus it is expected that the BH subsystem will be mass segregated. The expected mass fraction of stellar-mass BHs retained over time remains extremely uncertain due to poorly understood BH natal kicks from supernovae. Observationally, constraints on the BH kicks derived from the 3-D velocities of X-ray binaries suggest typical kicks > 100 km/s (Atri et al. 2019), with a small fraction having much lower kick velocities; these are perhaps BHs formed from direct collapse. The observed kicks are higher than expected from theoretical prescriptions that base the natal kicks on the better constrained neutron star kick distribution with a linear decrease in mass due to mass fall back and momentum conservation (e.g. Belczynski et al. 2002; Morscher et al. 2015; Banerjee et al. 2020; Mapelli 2021). The observed kick velocities are also above the escape velocities of even the most massive Milky Way clusters including ω Cen (Gnedin et al. 2002). In addition to uncertainties due to kicks, additional uncertainty on the retention fraction of stellar mass-BHs comes from the unknown initial conditions for clusters including the high-mass stellar initial mass function (e.g. Baumgardt & Hilker 2018), and the uncertainty in the initial-final mass relation of BHs (e.g. Spera et al. 2015; Mapelli 2021).

Models with $\sim 5\%$ of the cluster mass in segregated stellar mass BHs are able to explain the rise in the cen-

tral dispersion in ω Cen (Zocchi et al. 2019) and may be preferred to an IMBH model due to the lack of a high-velocity tail in the individual stellar velocities near the center (Baumgardt et al. 2019). An alternative constraint on BH mass fractions in Milky Way clusters was made by Weatherford et al. (2020) through modeling the observed mass segregation of stars. They constrained the BH mass fraction in Milky Way GCs, and found them to be $< 1\%$ in 48/50 clusters (including the massive clusters 47 Tuc and M54). They report a correlation between the BH mass fraction and the ratio of the core radius to the half-light radius, and find two clusters with $r_c/r_{hl} > 0.75$ to have BH mass fractions of up to 2%. **B023-G078's large r_c/r_{hl} thus suggests a high mass fraction of BHs may be present. We note that the tidal stripping of star clusters can also lead to very high BH mass fractions as stars are lost from the cluster faster than the mass-segregated BHs (Gieles et al. 2021).**

Relative to ω Cen, the higher metallicity of B023-G078 should lead to higher BH natal kicks (potentially lowering retention fractions) and lower typical BH masses and total BH mass fractions. To get a sense of the potential maximum mass fraction in BHs, we assumed a Kroupa (2001) IMF, the stellar evolution codes SSE & BSE using an $[\text{Fe}/\text{H}] = -0.7$ (Hurley et al. 2000, 2002) and the initial-final mass relations and BH kick prescriptions from (Banerjee et al. 2020). This combination yields a total initial mass in BHs of 4.3%, making up 7.8% of the final mass. **Removing BHs that receive kicks (and keeping only those that directly collapse), the present-day total mass fraction in BHs is 5.5%. As noted above, the retention of BHs is highly uncertain, and the kick prescription used here doesn't match that of observed X-ray binaries (Atri et al. 2019). On the other hand, the high mass of B023-G78 makes it plausible that a significant fraction of stellar-mass BHs are retained (e.g. Kremer et al. 2020).** Thus it appears possible that the inferred central IMBH in B023-G78 may instead be a collection of stellar mass BHs. **We examine this possibility further below.**

5.2.1. Testing the Stellar Mass BH Scenario with JAM Models

A collection of stellar-mass BHs differs from an IMBH because its mass distribution is extended, and this extent may be resolvable by our observations. In ω Cen, the best-fit distribution of stellar-mass BHs from Zocchi et al. (2019) can be described as a Plummer density profile ($\rho = 3M(1 + r^2/r_0^2)^{-5/2}/4\pi r_0^3$) with the ratio of the BH subsystem Plummer radius (r_0) to the cluster half-light radius (r_{hl}), (r_0/r_{hl}) ~ 0.3 . This ratio would correspond to a r_0 of ~ 1.3 pc ($0''.3$) in B023-G078; this is significantly broader than the core of our PSF and thus may result in measurable changes in our data relative to the point mass assumed in our IMBH models. However, we note that in the distribution function-based models of Zocchi et al. (2019), the amount of mass segregation between BHs and stars is fixed by a single parameter that is not well constrained, thus the ratio of (r_0/r_{hl}) is uncertain. A previous paper by Breen & Hoggie (2013) use theory, gas models, and N -body models on idealized clusters to understand the expected distribution of their

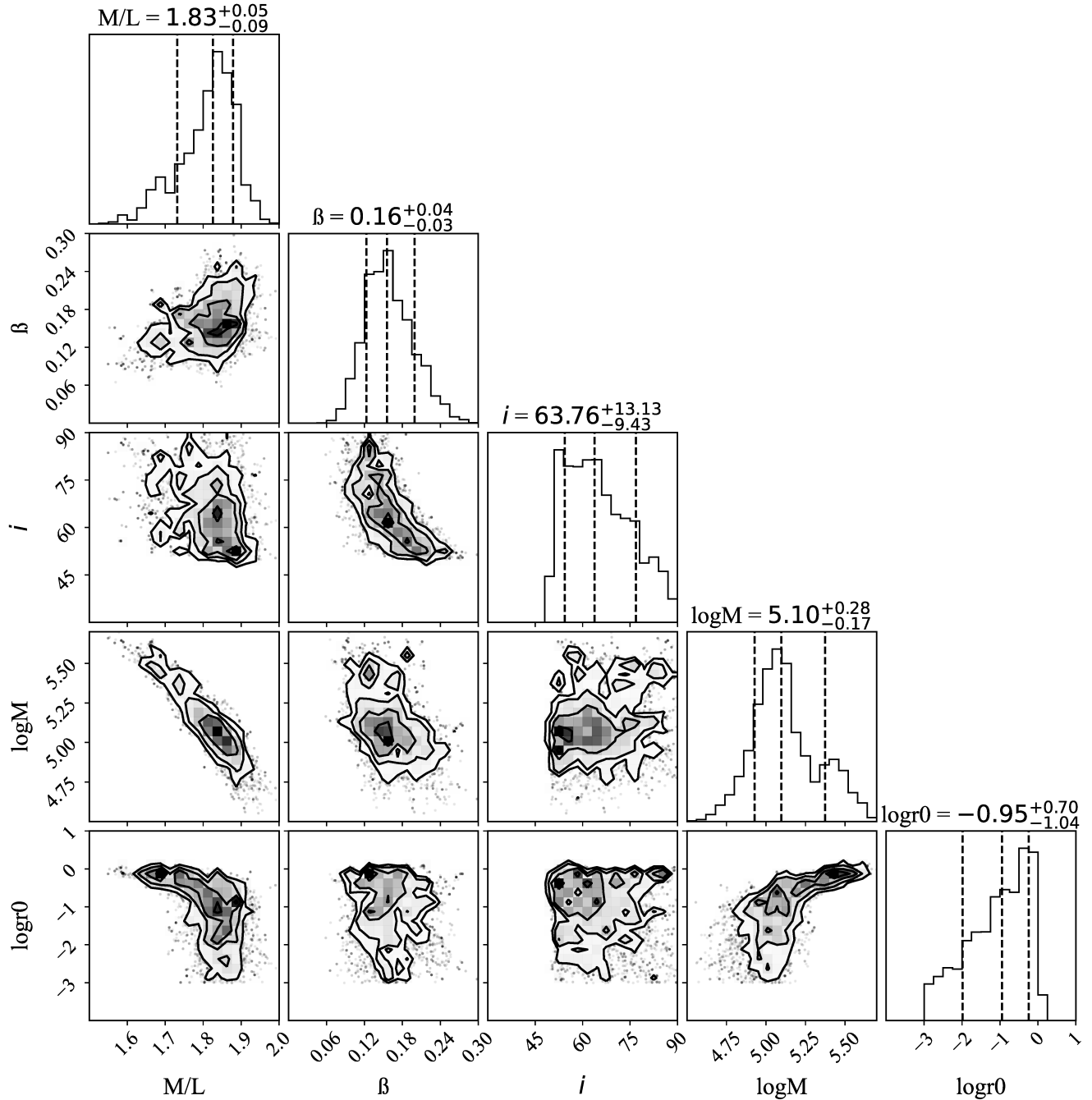


Figure 7. MCMC simulations of B023-G78 using a dark Plummer profile to describe a system of stellar mass BHs instead of an IMBH. The $\log M$ gives the total mass of the stellar mass BH subsystem, while $\log r_0$ indicates the Plummer radius, other parameters are the same as in Figure 4. The right two histograms give the best-fit “dark” component’s mass and size marginalized over all other parameters. The best-fit values of the total mass lie within 1σ of the IMBH mass in Figure 4, as do the inclination and anisotropy.

717 BHs; they find that for the parameters of ω Cen the ratio 727
 718 of half-mass radius of the BH sub-system ($r_{h,BH}$) over 728
 719 r_{hl} is $r_{h,BH}/r_{hl} \simeq 0.15$. This ratio depends on the BH 729
 720 mass fraction; for a mass ratio of $\sim 1\%$ as we find for 730
 721 the IMBH in B023-G078 they find $r_{h,BH}/r_h \simeq 0.1$. For a 731
 722 Plummer profile this translates to $r_0/r_{hl} \sim 0.08$, which in 732
 723 B023-G078 would give an r_0 of just 0.3 pc, or $0''.09$, only 733
 724 slightly larger than the PSF core Gaussian width of $0''.055$ 734
 725 making for a more challenging measurement. Thus, if a 735
 726 significant BH subsystem is present in B023-G078, it is 736

unclear whether we expect it to be significantly resolved by our observations.

To test whether an extended distribution of stellar mass BHs fits our kinematic data, we ran a new set of JAM models replacing the central BH with a “dark” Plummer density profile. To include this in our JAM models, we created an MGE for the Plummer profile and included the Plummer radius (r_0) and the total mass (M) as free parameters in our MCMC simulations along with M/L , inclination, and β . The results are shown in Fig-

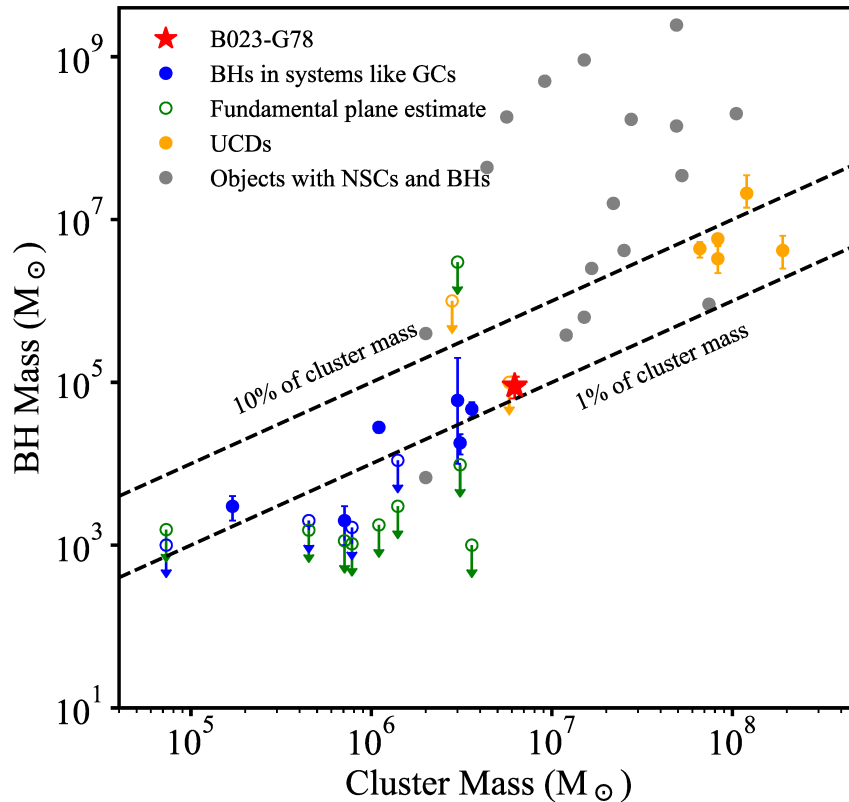


Figure 8. The black hole – cluster mass diagram for systems comparable to B023-G078BH. The blue data points are BH mass estimates in GCs from the compilation of [Greene et al. \(2020\)](#). The green data points are the fundamental plane upper limits of the same clusters from the same compilation. The orange points are stripped nuclei (UCDs) from ([Seth et al. 2014](#); [Ahn et al. 2017, 2018](#); [Voggel et al. 2018](#); [Afanasyev et al. 2018](#)). The gray points are the objects that have an estimate of both the BH and NSC mass from the compilation in [Neumayer et al. \(2020\)](#). All the open circles are upper limits. The dashed lines show BH masses that are 1% and 10% of their cluster mass. B023-G78 is the highest mass BH detected in a cluster below $10^7 M_{\odot}$.

737 ure 7. From our simulations, we find that the median
738 total mass of the dark component ($\sim 1.3 \times 10^5$) is within
739 $\sim 1\sigma$ of our estimate for the IMBH. The median of the
740 posterior for the Plummer r_0 parameter was ~ 0.11 pc
741 ($0''.03$) making it unresolved at our resolution; the best-
742 fit value of 0.09 pc is also consistent with this small and
743 unresolved r_0 . The 95% confidence upper limit on r_0 is
744 0.56 pc, thus the upper limit on r_0/r_{hl} is 0.13. The mass
745 of the dark system increases with increasing size, and for
746 the r_0 upper limit, the corresponding upper limit on the
747 total mass of the BH subsystem is $2 \times 10^5 M_{\odot}$, 3.2% of
748 the total system mass.

749 We also estimated the BIC for the IMBH simulations
750 and the models with the Plummer profile. We find a
751 ΔBIC of 6.3 providing positive evidence in favor of the
752 IMBH models. Combining this with the considerable
753 evidence that B023-G078 is a stripped NSC, we, there-
754 fore, favor an IMBH interpretation for our observations.
755 However, a compact system of stellar mass BHs is also a
756 possible explanation for the observed rise in the central
757 dispersion, as long as the $r_0 < 0.56$ pc and the total mass
758 in the BH subsystem is $\lesssim 3\%$.

759 We note that it is possible that both an IMBH and
760 a significant population of mass segregated stellar mass
761 BHs are present. A central BH significantly slows the

Table 3
Summary of results

| | IMBH | No-BH | Plummer |
|---------------------------------|---------------------------------|------------------------|---------------------------------|
| | model | model | model |
| M_{BH} (M_{\odot}) | $9.1^{+2.6}_{-2.8} \times 10^4$ | – | $1.3^{+1.1}_{-0.4} \times 10^5$ |
| M/L (M_{\odot}/L_{\odot}) | $1.87^{+0.04}_{-0.04}$ | $1.99^{+0.02}_{-0.02}$ | $1.83^{+0.05}_{-0.09}$ |
| β | $0.15^{+0.06}_{-0.04}$ | $0.22^{+0.04}_{-0.04}$ | $0.16^{+0.04}_{-0.03}$ |
| i | 64^{+18}_{-15} | 59^{+16}_{-7} | 64^{+13}_{-9} |
| r_0 (pc) | – | – | 0.09 |
| r_0 upper limit (pc) | – | – | 0.56 |
| Best-fit χ^2 | 404 | 434 | 404 |

Note: The best-fit parameters from the three different models we fit to the cluster.

762 process of mass segregation but does not completely halt
763 it ([Antonini 2014](#)). While we do not model this hybrid
764 case here, the constraints on the total mass of the dark
765 Plummer model above likely give an upper limit on the
766 mass of the stellar mass BH subsystem, even in the case
767 of co-existence with an IMBH. We summarize the results
768 and the properties of B023-G078 in Table 3 and Table 4.

Table 4
B023-G078 cluster properties

| | |
|---------------------------|--|
| Central V_{RMS} | 37.2±0.6 km/s |
| V/σ | 0.8 |
| Cluster mass | $6.22^{+0.03}_{-0.02} \times 10^6 M_{\odot}$ |
| BH Mass | $9.1^{+2.6}_{-2.8} \times 10^4 M_{\odot}$ |
| BH mass fraction | 1.5% |
| Half-mass relaxation time | 14 Gyr |
| $[Fe/H]$ | -0.65 (center) to -0.80 (at 1") |
| Age | 10.5 ± 0.5 Gyr |
| Assumed E(B-V) | 0.23 |

Note: B023-G078 properties that we derived from our analyses. The E(B-V) value is from [Jablonka et al. \(1992\)](#) and used as a default value in this paper.

5.3. B023-G78 in Context

Assuming our observed dynamical signature is an IMBH, we consider how it compares to other IMBH candidates and UCD/BH systems in Fig. 8. At the lower mass end, a comparison sample of claimed dynamical detections of massive BHs in GCs, as well as published upper limits for the same clusters are shown from the recent compilation of [Greene et al. \(2020\)](#). We note many of the dynamical detections plotted here are disputed and refer readers to [Greene et al. \(2020\)](#) for details. In addition we add higher mass UCDs from recent discoveries, as well as present-day galaxies with both NSCs and BHs to provide context.

Relative to any other Local Group star cluster, the $\sim 9 \times 10^4 M_{\odot}$ BH in B023-G78 is the highest mass detection claimed, double the suggested mass of the BH in ω Cen (e.g. [Noyola et al. 2010](#)); as noted previously this IMBH detection has been contested (e.g. [Zocchi et al. 2017, 2019; Baumgardt et al. 2019](#)). It is also more significant than the $< 3\sigma$ detection of a $2 \times 10^4 M_{\odot}$ BH in G1 ([Gebhardt et al. 2005](#)) derived from data with similar physical resolution.

In comparison with the BHs previously found in other higher-mass UCDs, B023-G78 represents the first case in the IMBH regime, with all other BHs having both higher masses and mass fractions. Relative to central BHs in present-day galaxies, the mass is the lowest dynamical estimate apart from the $\sim 10^4 M_{\odot}$ BH suggested in NGC 205 ([Nguyen et al. 2019](#)). The most comparable present-day NSC+BH system is NGC 4395, which hosts a $\sim 4 \times 10^5 M_{\odot}$ BH, inferred both dynamically ([den Brok et al. 2015](#)) and from reverberation mapping (e.g. [Peterson et al. 2005](#)), that lies in a $\sim 2 \times 10^6 M_{\odot}$ NSC ([den Brok et al. 2015](#)). The inferred IMBH in B023-G78 is also comparable to the lowest mass BHs inferred from accretion (e.g. [Baldassare et al. 2015; Chilingarian et al. 2018](#)).

We also checked for possible BH accretion signatures in B023-G078. There is no cataloged X-ray source matching the location of B023-G078 in the deep XMM mosaic of [Stiele et al. \(2011\)](#). The faintest cataloged sources close to the location of B023-G078 have 0.5–4.5 keV XMM/EPIC unabsorbed fluxes of $2.1 \times 10^{-14} \text{ erg s}^{-1} \text{ cm}^{-2}$, which corresponds to a 0.5–10 keV X-ray luminosity of $1.9 \times 10^{35} \text{ erg}^{-1}$ assuming a photon index of

$\Gamma = 1.7$. Hence the non-detection of B023-G078 in these data suggests a 0.5–10 keV upper limit of $L_X \lesssim 2 \times 10^{35} \text{ erg}^{-1}$. Using this upper limit to the X-ray luminosity in B023-G078 combined with our derived dynamical BH mass, the predicted 5 GHz luminosity is $< 8.5 \mu\text{Jy}$ ([Plotkin et al. 2012](#)). B023-G078 is not detected in VLASS, and with an RMS noise in the VLASS image of $127 \mu\text{Jy}/\text{bm}$, we can estimate a $3\text{-}\sigma$ upper limit of $< 381 \mu\text{Jy}$. Therefore, in this case the X-ray limit (if accurate) is much more constraining than the radio data, although it would be possible to get significantly deeper radio data. We also note that the presence of stellar mass black holes could also lead to detectable X-ray binaries, as B023-G078 does have a very high collision rate. However, among the highest collision rate GCs in M31 only a fraction ($< \text{half}$) appear to have bright X-ray sources (e.g., [Peacock et al. 2010](#)). We note in this context that in ω Cen, which as discussed above, may host a large cluster of stellar mass BHs ([Zocchi et al. 2019; Baumgardt et al. 2019](#)). However, no bright X-ray binaries are found, with the brightest X-ray sources being $< 10^{33} \text{ ergs/s}$ ([Henleywillis et al. 2018](#)).

One potentially comparable systems detected via accretion is HLX-1, a bright off-nuclear X-ray source with an inferred BH mass of $10^{4-5} M_{\odot}$ (e.g. [Webb et al. 2012](#)). Due to the light from HLX-1 itself, constraining the age and mass of the surrounding stellar cluster is challenging (e.g. [Soria et al. 2010; Farrell et al. 2014; Soria et al. 2017](#)), but if it is old, its mass is estimated to be $\sim 3 \times 10^6 M_{\odot}$ ([Soria et al. 2017](#)).

6. CONCLUSIONS

We have presented adaptive-optics GEMINI/NIFS IFU kinematic data of M31's most massive star cluster, B023-G78. We combined these data with mass models derived from HST ACS/HRC to constrain the mass content, including a possible central black hole in this massive star cluster. We find the following:

1. The kinematics of B023-G78 show a rise in the integrated velocity dispersion to ~ 37 km/s, and a peak rotation of ~ 20 km/s.
2. The surface brightness profile requires at least two components to fit, and shows a small color gradient, with the outer component being ~ 0.05 mags bluer than the inner component. A significant metallicity gradient of ~ 0.15 dex is also seen within the central arcsecond.
3. Our best-fit JAM dynamical models give a BH mass of $9.1^{+2.6}_{-2.8} \times 10^4 M_{\odot}$, M/L_{F814W} of $1.87^{+0.04}_{-0.04}$ and anisotropy $0.15^{+0.06}_{-0.04}$. The BH detection is highly significant $> 3\sigma$, and systematic errors are $< 10\%$ on the best-fit BH mass.

We discuss the possibility that this BH can be explained due to a collection of dark stellar remnants, and constrain the extent of these remnants and find the derived extent of the dark remnants are mostly unresolved by our observations, with an upper limit on the Plummer r_0 of 0.56 pc. We favor the presence of a single

875 IMBH given the other indications that B023-G78 is a
876 stripped nucleus, as well as the apparent compactness
877 of the dark component. Higher spatial-resolution data
878 would give improved constraints on the nature of the
879 central dark mass and should be a high priority in the
880 forthcoming era of extremely large telescopes.

881 The authors thank Mark Gieles and Alice Zocchi for
882 useful conversations about this work. R.P. and A.C.S ac-
883 knowledge support from grants NSF AST-1350389 and
884 AST-1813708. N.N. gratefully acknowledges support
885 by the Deutsche Forschungsgemeinschaft (DFG, German
886 Research Foundation) – Project-ID 138713538 – SFB
887 881 (“The Milky Way System”, subproject B8). R.P.
888 and S.K. gratefully acknowledge funding from UKRI
889 in the form of a Future Leaders Fellowship (grant no.
890 MR/T022868/1. JS acknowledges support from NSF
891 grant AST-1812856 and the Packard Foundation. This
892 paper is based on observations obtained at the interna-
893 tional Gemini Observatory, a program of NSF’s NOIR-
894 Lab, which is managed by the Association of Universi-
895 ties for Research in Astronomy (AURA) under a cooper-
896 ative agreement with the National Science Foundation.
897 on behalf of the Gemini Observatory partnership: the
898 National Science Foundation (United States), National
899 Research Council (Canada), Agencia Nacional de Inves-
900 tigación y Desarrollo (Chile), Ministerio de Ciencia, Tec-
901 nología e Innovación (Argentina), Ministério da Ciência,
902 Tecnologia, Inovações e Comunicações (Brazil), and Ko-
903 rean Astronomy and Space Science Institute (Republic of
904 Korea).

REFERENCES

906 Afanasiev, A. V., Chilingarian, I. V., Mieske, S., et al. 2018,
907 MNRAS, 477, 4856
908 Ahn, C. P., Seth, A. C., den Brok, M., et al. 2017, ApJ, 839, 72
909 Ahn, C. P., Seth, A. C., Cappellari, M., et al. 2018, ApJ, 858, 102
910 Alfaro-Cuello, M., Kacharov, N., Neumayer, N., et al. 2019, ApJ,
911 886, 57
912 Anderson, J., & van der Marel, R. P. 2010, ApJ, 710, 1032
913 Antonini, F. 2014, ApJ, 794, 106
914 Ashok, A., Zasowski, G., Seth, A., et al. 2021, AJ, 161, 167
915 Atri, P., Miller-Jones, J. C. A., Bahramian, A., et al. 2019,
916 MNRAS, 489, 3116
917 Baldassare, V. F., Reines, A. E., Gallo, E., & Greene, J. E. 2015,
918 ApJ, 809, L14
919 Banerjee, S., Belczynski, K., Fryer, C. L., et al. 2020, A&A, 639,
920 A41
921 Barmby, P., Huchra, J. P., & Brodie, J. P. 2001, AJ, 121, 1482
922 Barmby, P., McLaughlin, D. E., Harris, W. E., Harris, G. L. H.,
923 & Forbes, D. A. 2007, AJ, 133, 2764
924 Bastian, N., & Lardo, C. 2018, ARA&A, 56, 83
925 Baumgardt, H. 2017, MNRAS, 464, 2174
926 Baumgardt, H., & Hilker, M. 2018, MNRAS, 478, 1520
927 Baumgardt, H., Makino, J., Hut, P., McMillan, S., & Portegies
928 Zwart, S. 2003, ApJ, 589, L25
929 Baumgardt, H., He, C., Sweet, S. M., et al. 2019, MNRAS, 488,
930 5340
931 Belczynski, K., Kalogera, V., & Bulik, T. 2002, ApJ, 572, 407
932 Breen, P. G., & Heggie, D. C. 2013, MNRAS, 432, 2779
933 Bressan, A., Marigo, P., Girardi, L., et al. 2012, MNRAS, 427, 127
934 Caldwell, N., Schiavon, R., Morrison, H., Rose, J. A., & Harding,
935 P. 2011, AJ, 141, 61
936 Cappellari, M. 2002, MNRAS, 333, 400
937 —. 2008, MNRAS, 390, 71
938 —. 2017, MNRAS, 466, 798
939 Cappellari, M., & Copin, Y. 2003, MNRAS, 342, 345
940 Chilingarian, I. V., Katkov, I. Y., Zolotukhin, I. Y., et al. 2018,
941 ApJ, 863, 1
942 Davis, S. W., Narayan, R., Zhu, Y., et al. 2011, ApJ, 734, 111
943 Davis, T. A., Nguyen, D. D., Seth, A. C., et al. 2020, MNRAS,
944 496, 4061
945 den Brok, M., van de Ven, G., van den Bosch, R., & Watkins, L.
946 2014, MNRAS, 438, 487

den Brok, M., Seth, A. C., Barth, A. J., et al. 2015, ApJ, 809, 101
Erwin, P. 2015, ApJ, 799, 226
Farrell, S. A., Servillat, M., Gladstone, J. C., et al. 2014,
949 MNRAS, 437, 1208
950 Foreman-Mackey, D., Hogg, D. W., Lang, D., & Goodman, J.
951 2013, Publications of the Astronomical Society of the Pacific,
952 125, 306–312
953 Fuentes-Carrera, I., Jablonka, P., Sarajedini, A., et al. 2008,
954 A&A, 483, 769
955 Gebhardt, K., Rich, R. M., & Ho, L. C. 2002, ApJ, 578, L41
956 —. 2005, ApJ, 634, 1093
957 Gebhardt, K., Bender, R., Bower, G., et al. 2000, ApJ, 539, L13
958 Gieles, M., Erkal, D., Antonini, F., Balbinot, E., & Peñarrubia, J.
959 2021, arXiv e-prints, arXiv:2102.11348
960 Gnedin, O. Y., Zhao, H., Pringle, J. E., et al. 2002, ApJ, 568, L23
961 Godet, O., Plazolles, B., Kawaguchi, T., et al. 2012, ApJ, 752, 34
962 Gonzaga et al., S. 2012, The DrizzlePac Handbook
963 Graham, A. W., & Driver, S. P. 2005, PASA, 22, 118
964 Greene, J. E., Strader, J., & Ho, L. C. 2020, ARA&A, 58, 257
965 Henleywillis, S., Cool, A. M., Haggard, D., et al. 2018, MNRAS,
966 479, 2834
967 Hurley, J. R., Pols, O. R., & Tout, C. A. 2000, MNRAS, 315, 543
968 Hurley, J. R., Tout, C. A., & Pols, O. R. 2002, MNRAS, 329, 897
969 Husser, T. O., Wende-von Berg, S., Dreizler, S., et al. 2013, A&A,
970 553, A6
971 Ibata, R., Bellazzini, M., Chapman, S. C., et al. 2009, ApJ, 699,
972 L169
973 Jablonka, P., Alloin, D., & Bica, E. 1992, A&A, 260, 97
974 Janz, J., Norris, M. A., Forbes, D. A., et al. 2016, MNRAS, 456,
975 617
976 Johnson, C. I., & Pilachowski, C. A. 2010, ApJ, 722, 1373
977 Kamann, S. 2018, PampelMuse: Crowded-field 3D spectroscopy,
978 ascl:1805.021
979 Kamann, S., Wisotzki, L., & Roth, M. M. 2013, A&A, 549, A71
980 Karachentsev, I. D., Karachentseva, V. E., Huchtmeier, W. K., &
981 Makarov, D. I. 2004, AJ, 127, 2031
982 Kass, R. E., & Raftery, A. E. 1995, Journal of the American
983 Statistical Association, 90, 773
984 King, I. 1962, AJ, 67, 471
985 Kremer, K., Ye, C. S., Rui, N. Z., et al. 2020, ApJS, 247, 48
986 Kroupa, P. 2001, MNRAS, 322, 231
987 Lützgendorf, N., Gebhardt, K., Baumgardt, H., et al. 2015, A&A,
988 581, A1
989 Majewski, S. R., Nidever, D. L., Smith, V. V., et al. 2012, ApJ,
990 747, L37
991 Mapelli, M. 2021, arXiv e-prints, arXiv:2106.00699
992 McConnell, N. J., & Ma, C.-P. 2013, ApJ, 764, 184
993 Mezcua, M., Civano, F., Marchesi, S., et al. 2018, MNRAS, 478,
994 2576
995 Mieske, S., Frank, M. J., Baumgardt, H., et al. 2013, A&A, 558,
996 A14
997 Miller-Jones, J. C. A., Wrobel, J. M., Sivakoff, G. R., et al. 2012,
998 ApJ, 755, L1
999 Monaco, L., Bellazzini, M., Ferraro, F. R., & Pancino, E. 2005,
1000 MNRAS, 356, 1396
1001 Morscher, M., Pattabiraman, B., Rodriguez, C., Rasio, F. A., &
1002 Umbreit, S. 2015, ApJ, 800, 9
1003 Myeong, G. C., Vasiliev, E., Iorio, G., Evans, N. W., &
1004 Belokurov, V. 2019, MNRAS, 488, 1235
1005 Neumayer, N., Seth, A., & Böker, T. 2020, A&A Rev., 28, 4
1006 Nguyen, D. D., Seth, A. C., Neumayer, N., et al. 2018, ApJ, 858,
1007 118
1008 —. 2019, ApJ, 872, 104
1009 Noyola, E., Gebhardt, K., Kissler-Patig, M., et al. 2010, ApJ, 719,
1010 L60
1011 Peacock, M. B., Maccarone, T. J., Knigge, C., et al. 2010,
1012 MNRAS, 402, 803
1013 Pechetti, R., Seth, A., Neumayer, N., et al. 2020, ApJ, 900, 32
1014 Peng, C. Y., Ho, L. C., Impey, C. D., & Rix, H.-W. 2010, AJ,
1015 139, 2097
1016 Perina, S., Federici, L., Bellazzini, M., et al. 2009, A&A, 507, 1375
1017 Peterson, B. M., Bentz, M. C., Desroches, L.-B., et al. 2005, ApJ,
1018 632, 799
1019 Pfeffer, J., & Baumgardt, H. 2013, MNRAS, 433, 1997
1020 Pfeffer, J., Lardo, C., Bastian, N., Saracino, S., & Kamann, S.
1021 2021, MNRAS, 500, 2514
1022 Plotkin, R. M., Markoff, S., Kelly, B. C., KÖrding, E., &
1023 Anderson, S. F. 2012, MNRAS, 419, 267
1024 Reines, A. E., Greene, J. E., & Geha, M. 2013, ApJ, 775, 116
1025 Roediger, J. C., & Courteau, S. 2015, MNRAS, 452, 3209
1026 Saglia, R. P., O’pitsch, M., Erwin, P., et al. 2016, ApJ, 818, 47
1027 Sarajedini, A., & Layden, A. C. 1995, AJ, 109, 1086
1028 Sersic, J. L. 1968, Atlas de Galaxias Australes
1029 Seth, A. C., Cappellari, M., Neumayer, N., et al. 2010, ApJ, 714,
1030 713
1031 Seth, A. C., van den Bosch, R., Mieske, S., et al. 2014, Nature,
1032 513, 398
1033

- 1034 Siegel, M. H., Dotter, A., Majewski, S. R., et al. 2007, *ApJ*, 667, 1046
 1035 L57 1047
- 1036 Simpson, J. D., Martell, S. L., Da Costa, G., et al. 2020, *MNRAS*, 1048
 1037 491, 3374 1049
- 1038 Soria, R., Hau, G. K. T., Graham, A. W., et al. 2010, *MNRAS*, 1050
 1039 405, 870 1051
- 1040 Soria, R., Musaeva, A., Wu, K., et al. 2017, *MNRAS*, 469, 886 1052
- 1041 Spera, M., Mapelli, M., & Bressan, A. 2015, *MNRAS*, 451, 4086 1053
- 1042 Stiele, H., Pietsch, W., Haberl, F., et al. 2011, *A&A*, 534, A55 1054
- 1043 Strader, J., Caldwell, N., & Seth, A. C. 2011, *AJ*, 142, 8 1055
- 1044 Straub, O., Godet, O., Webb, N., Servillat, M., & Barret, D. 1056
 1045 2014, *A&A*, 569, A116
- Suntzeff, N. B., & Kraft, R. P. 1996, *AJ*, 111, 1913
- Tremou, E., Strader, J., Chomiuk, L., et al. 2018, *ApJ*, 862, 16
- Voggel, K. T., Seth, A. C., Baumgardt, H., et al. 2019, *ApJ*, 871, 159
- Voggel, K. T., Seth, A. C., Neumayer, N., et al. 2018, *ApJ*, 858, 20
- Weatherford, N. C., Chatterjee, S., Kremer, K., & Rasio, F. A. 2020, *ApJ*, 898, 162
- Webb, N., Cseh, D., Lenc, E., et al. 2012, *Science*, 337, 554
- Zocchi, A., Gieles, M., & Hénault-Brunet, V. 2017, *MNRAS*, 468, 4429
- . 2019, *MNRAS*, 482, 4713